Distributed Continuous-time Unit Commitment with Energy Storage in Multi-area Networks

Bishal Lamichhane[a], Yu Christine Chen[b], Alfredo Garcia[c]

[a] *Southern Illinois University, Illinois, USA*
[b] *The University of British Columbia, British Columbia, Canada*
[c] *Texas A & M University, Texas, USA*

Abstract

This paper proposes a distributed solution for multi-area unit commitment (UC) problem with continuous-time energy generation and storage, offering an enhanced operation tool that leverages the available operational flexibility resources via higher fidelity modeling to enable effective resource sharing among areas via coordinated continuous-time interconnection power exchange. The proposed methodology involves formulating a variational multi-area UC problem with energy storage where decision variables (including power, energy, and commitment statuses) are modeled as continuous-time trajectories and ramping is defined as the time-derivative of the respective power trajectory. The variational multi-area UC problem is then projected into Bernstein function space, leading to a mixed-integer linear programming (MILP) problem with Bernstein coefficients of dispatch and commitment status trajectories as decision variables. The function space-based multi-area UC problem is then decomposed into per-area UC sub-problems solved using a distributed algorithm. Implemented on two different test networks and compared against the benchmark centralized and traditional discrete-time solutions, the numerical results highlight the solution accuracy and efficacy of the proposed distributed method to achieve optimal decisions on interconnection power exchanges such that the energy and ramping needs of all participating areas are met.

Keywords: distributed optimization, multi-area unit commitment, energy storage, continuous-time scheduling

1. Introduction

Electric power systems are undergoing substantial changes due to integration of large-scale renewable energy sources (RESs) to meet ambitious targets for carbon emissions reduction [1, 2]. Despite their obvious environmental and economic benefits, RESs pose operational challenges due to variability and intermittency in power supply and increased likelihood of high ramping needs [3]. Imperative to fully realizing pertinent benefits of RESs while maintaining reliable power supply is to take advantage of flexibility offered by resources like energy storage (ES) devices and flexible loads, as well as to modernize the associated control and communication infrastructure [4, 5, 6]. Moreover, the growing need for seamless integration of distributed energy resources (DERs) and aggregators into power system operation models, as highlighted by recent policies [7] and reports [8], necessitates an upgrade to the current operational framework. A comprehensive review of emerging challenges in current electricity market and power system operation solution architectures, posed by the evolving generation and demand mix as well as the requirement of short-time interval scheduling, is provided in [9]. While a single, ideal solution to address the dynamic and evolving needs of modern power system operations may not yet be available, ongoing research is exploring a variety of methods and strategies to tackle both immediate and long-term challenges [10, 11]. This paper focuses on enhancing power system operation models to account for inter-temporal variability and adjusting market structures.

1.1. Related Work

The underlying optimization problem of power system operation models approximate the electric demand and generation with piecewise constant functions of equal length spanning the scheduling horizon (e.g., hourly piecewise constant functions for day-ahead scheduling horizon) [12]. Such operation models have proven effective under relatively smooth changes in net electric demand (demand minus non-dispatchable renewable generation). However, the performance of present operation models may diminish as large-scale renewable energy integration introduces greater variability to net demand, posing risk of ramping inadequacy in power systems.

Recent work tackling the challenge of ramping inadequacy and inter-temporal variability by providing various upgrades to power system operation models includes [13, 14], where a time-adaptive unit commitment (UC)

model unlocks greater operational flexibility by adjusting the scheduling time-interval lengths in response to net demand variations and resource types, respectively. Furthermore, [15] highlights the benefits of embedding continuous-time functions into optimization problems. This approach offers a more effective means to leverage the provided flexibility while maintaining controlled computational tractability, particularly as discrete time intervals become significantly small. In another work, [16] demonstrates the computational effectiveness of using continuous-time function space to model the inter-temporal flexibility of load aggregators and wind-power generation in the UC problem. In [17], piecewise constant functions are substituted by piecewise linear ones to enable trading of *power* instead of energy. More function space modeling approaches are presented in [18, 19, 20, 21, 22], where Bernstein splines of desired degrees replace the piecewise constant functions in the traditional UC formulation, the outcome being an optimization problem with Bernstein coefficients of generation trajectories as decision variables. By explicitly defining the ramping trajectories as time-derivatives of continuous-time power trajectories, the function space-based method in [18, 19, 20, 21, 22] can accurately evaluate the net demand ramping requirement and supplies it by tapping into the available flexibility resources in the grid, leading to a closely approximated continuous-time generation schedule with little increase in computation efforts.

While the aforementioned studies present a strong case for continuous-time modeling as an alternative to conventional discrete-time approaches for addressing variability and flexibility, their application in electricity market structures for multi-area interconnected power systems is not fully investigated, especially in the context of integrating many distributed energy resources.

The term "multi-area interconnected power systems" refers to a setup of independent grids (referred as *areas* in this paper) exchanging power through tielines to improve system reliability and economics [23]. For example, Independent System Operators (ISOs) operate wholesale electricity markets within regional power grids while maintaining interconnections with neighboring ISOs and grids through multiple tielines, facilitating resource sharing and coordination [24]. ISOs are often divided into multiple internal sub-areas, such as capacity zones, key study areas, system planning sub-areas, and Distribution System Operators (DSOs). Each serves specific purposes, including optimizing resource allocation, improving grid reliability, and supporting system planning.

While electricity market operators typically handle optimal generation scheduling as a single optimization problem, there is growing interest in finding alternatives due to concerns over data privacy and cybersecurity risks from large-scale data exchange in centralized systems [25], as well as challenges in integrating small DERs and load aggregators into these centralized market solutions [8]. Among various emerging solutions, [26] suggests that a differential privacy-based privacy-preserving mechanism could be implemented in centralized electricity markets and highlights its potential applicability in alternating direction method of multipliers (ADMM)-based distributed settings. Alternatively, [27] highlights data privacy concerns in centralized market structures and proposes a day-ahead distributed market solution using optimality condition decomposition (OCD) as a more effective approach. When tested on the IEEE-RTS, this solution achieved similar results to the centralized benchmark while ensuring privacy. Likewise, [28] proposes an ADMM-based bi-level distributed day-ahead scheduling model for islanded multi-microgrids in a carbon trading market, emphasizing data privacy and reduced communication burden, while demonstrating ADMM's ability to find the global optimal solution of the upper level in a distributed manner. Additionally, [29] addresses data privacy and centralized operation concerns for ISOs in multi-area interconnected power systems by using ADMM combined with the regularized primal-dual interior point method to iteratively solve a distributed nonconvex AC security-constrained UC problem.

Other recent work further emphasizes decomposition techniques as viable privacy-preserving solutions to the multi-area UC problem [30, 31, 32, 33, 34]. A comprehensive review of distributed/decentralized solutions for the UC problem is presented in [30], identifying dual decomposition (DP), ADMM, auxiliary problem principle (APP), and analytical target cascading (ATC), as four major algorithms adopted in prior works. While dual decomposition based decentralized framework for UC is deemed practically inefficient due to higher computation time, distributed frameworks based on ADMM, APP, and ATC have been proposed in their standard and modified forms in prior studies, demonstrating convergence of the algorithm to a local solution [30]. In [31], a decentralized UC problem is formulated for a large-scale power system within ADMM framework, aided by refinements and heuristics to mitigate oscillations and avoid local optima which could result from nonconvexity of the UC problem. The multi-area UC problem in the presence of wind power uncertainty is formulated as a decentralized optimization

problem in [32] and the optimal interconnection power exchange along with geographical allocation of required reserve are determined using the APP algorithm. Aimed at alleviating the computational burden, [33] proposes a distributed ATC-based solution facilitated by a central coordinator to solve the UC problem for large-scale power networks by virtually decomposing them into multiple scalable zones, and a decentralized variation that removes the central coordinator is presented in [34] to address more stringent privacy requirements.

1.2. Summary of Contributions

Despite the strides made in advancing distributed/decentralized solutions for the traditional multi-area UC problem, none have been applied to variational multi-area UC problem with continuous-time decision trajectories, missing out on benefits offered by function space-based modeling. In this paper, we extend our preliminary work [35] and the function space-based modeling approach to address a gap in the literature by proposing a computationally efficient, function space-based distributed solution for the continuous-time UC problem in multi-area networks, specifically applicable to day-ahead power system operation models. The solution enables continuous-time power exchange between interconnected areas, leverages enhanced operational flexibility through higher fidelity modeling, supports integration of distributed energy storage systems at the local level, and retains the data privacy and computational benefits of distributed optimization approaches.

Distinct from [35] that develops a distributed solution for the continuous-time optimal power flow (OPF) problem assuming predetermined commitment statuses for generators and excluding ES devices from the generation fleet, the current effort tackles the more involved UC problem incorporating binary commitment status decisions and co-optimizing energy generation and storage. Also unlike [35], the proposed model embeds a broader set of generator technical limitations including startup and shutdown costs and minimum up and down time constraints, and enables sharing the ramping flexibility offered by fast-ramping units and ES devices among interconnected areas, thus enhancing the overall efficiency of the entire network. Finally, different from [35] that employs the ADMM, we adopt an ATC algorithm, known to offer greater flexibility than ADMM and APP algorithms for solving the UC problem in terms of sub-problem coordination and penalty function selection [33, 34]. The implementation of the proposed ATC-based distributed solution on the three-area IEEE Reliability Test System (IEEE-RTS) and a larger

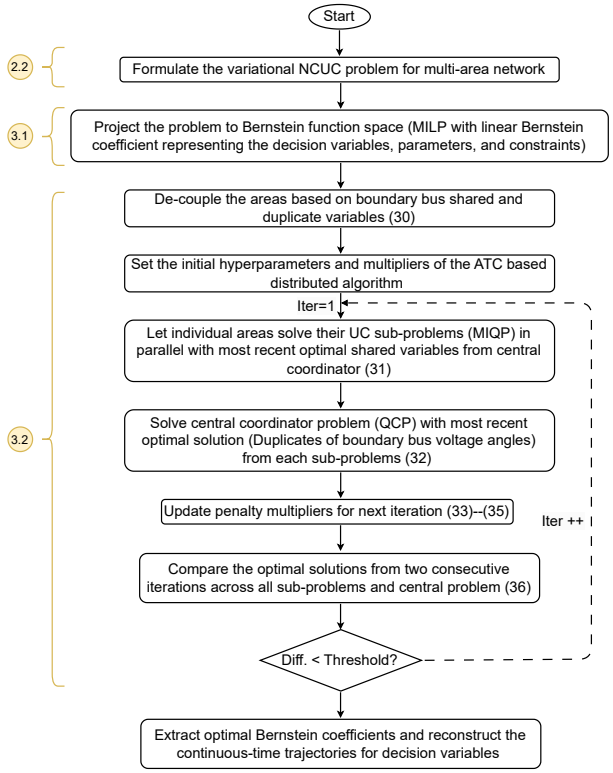

Figure 1: Flow diagram of the proposed solution methodology.

six-area network demonstrates the performance of the proposed approach in terms of solution accuracy and scalability, as well as its ability to achieve optimal resource sharing among areas through interconnection power exchange with higher granularity compared to discrete-time interval UC models.

The remainder of this paper is organized as follows. Section 2 is dedicated to preliminaries including the multi-area transmission network model and the variational multi-area UC problem formulation. The proposed solution methodology is presented in Section 3, where the function space representation and distributed solution are presented. Numerical results are provided in Section 4. Finally, we offer concluding remarks in Section 5.

2. Methodology Overview and Preliminaries

The overall methodology of this paper illustrated in Fig. 1 involves formulating the multi-area network constrained unit commitment (NCUC) problem with thermal generating units and ES devices as a variational optimization

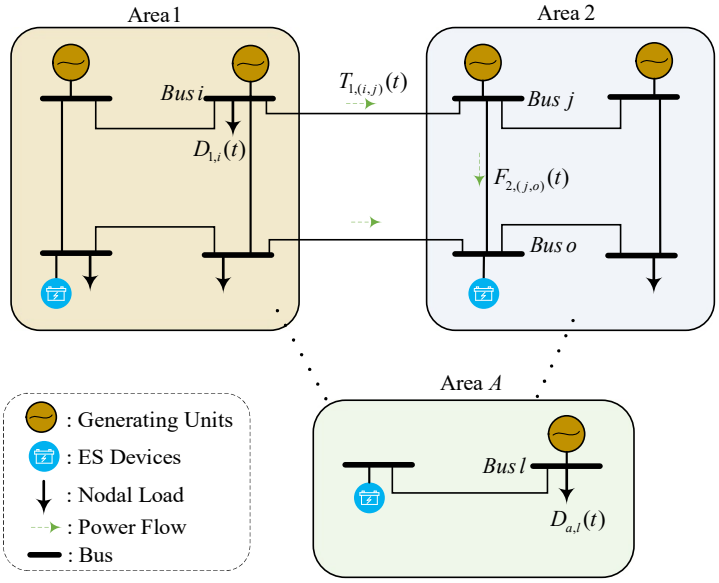

Figure 2: Generic multi-area power transmission network.

problem, followed by projecting the decision trajectories and operational constraints into Bernstein function space through which the original variational problem converts to a mixed-integer linear programming (MILP) problem with Bernstein coefficients of dispatch and commitment status trajectories as decision variables, and subsequent distributed solution via an ATC algorithm. We next present components of the multi-area transmission network model followed by the variational multi-area UC problem formulation.

2.1. Multi-area Transmission Network

Consider a power transmission network with A areas collected in the set $\mathcal{A} = \{1, \ldots, A\}$, as shown in Fig. 2. Each area $a \in \mathcal{A}$ is modeled as a directed graph $(\mathcal{N}_a, \mathcal{L}_a)$, where $\mathcal{N}_a = \{1, \ldots, N_a\}$ and $\mathcal{L}_a = \{(i,j) \,|\, i,j \in \mathcal{N}_a, j \equiv j(i)\}$ respectively represent the sets of nodes (buses) and edges (transmission lines). Furthermore, the set $\mathcal{L}_a^{\text{tie}} = \{(i,j) \,|\, i \in \mathcal{N}_a, j \in \mathcal{N}_{\hat{a}}, j \equiv j(i)\}$ collects tielines originating from area a. At each time t within the scheduling horizon $\mathcal{T} = [0, T]$, nodal loads in area a are collected in vector[1] $D_a(t) = [(D_{a,n}(t))_{n \in \mathcal{N}_a}]^{\mathrm{T}}$. These loads are served by K_a generating units along with R_a ES devices, respectively contained in sets $\mathcal{K}_a = \{1, \ldots, K_a\}$ and $\mathcal{R}_a = \{1, \ldots, R_a\}$,

[1]All vector variables are column vectors unless otherwise specified.

and possibly by imports provided by neighboring areas. The power generation trajectories of units are collected in vector $G_a(t) = [(G_{a,k}(t))_{k\in\mathcal{K}_a}]^{\mathrm{T}}$, their ramping trajectories are defined as the time-derivatives of corresponding power trajectories and included in vector $\dot{G}_a(t) = [(\dot{G}_{a,k}(t))_{k\in\mathcal{K}_a}]^{\mathrm{T}}$, and their commitment status trajectories form the vector $I_a(t) = [(I_{a,k}(t))_{k\in\mathcal{K}_a}]^{\mathrm{T}}$. The charging (discharging) power of ES devices form the vector $D_a^{\mathrm{es}}(t) = [(D_{a,r}^{\mathrm{es}}(t))_{r\in\mathcal{R}_a}]^{\mathrm{T}}$ ($G_a^{\mathrm{es}}(t) = [(G_{a,r}^{\mathrm{es}}(t))_{r\in\mathcal{R}_a}]^{\mathrm{T}}$), the corresponding charging (discharging) ramping trajectories are collected in vector $\dot{D}_a^{\mathrm{es}}(t) = [(\dot{D}_{a,r}^{\mathrm{es}}(t))_{r\in\mathcal{R}_a}]^{\mathrm{T}}$ ($\dot{G}_a^{\mathrm{es}}(t) = [(\dot{G}_{a,r}^{\mathrm{es}}(t))_{r\in\mathcal{R}_a}]^{\mathrm{T}}$), and their stored energy form the vector $E_a^{\mathrm{es}}(t) = [(E_{a,r}^{\mathrm{es}}(t))_{r\in\mathcal{R}_a}]^{\mathrm{T}}$. The area nodal voltage phase-angle trajectories are collected in vector $\theta_a(t) = [(\theta_{a,n}(t))_{n\in\mathcal{N}_a}]^{\mathrm{T}}$, transmission line (tieline) power flows form the vector $F_a(t) = [(F_{a,(i,j)}(t))_{(i,j)\in\mathcal{L}_a}]$ ($T_a(t) = [(T_{a,(i,j)}(t))_{(i,j)\in\mathcal{L}_a^{\mathrm{tie}}}]$). Finally, B_a denotes the $N_a \times N_a$ susceptance matrix for area a.

2.2. Variational Multi-area Unit Commitment Problem

We formulate the centralized variational UC problem as in [21], under the assumption that a single system operator has complete information of the entire interconnected network. We minimize the total operation cost of the power system, consisting of generation costs $C_a(G_a(t)) = \sum_{k\in\mathcal{K}_a} C_{a,k}(G_{a,k}(t))$ and startup and shutdown costs $SU_a(t) = [(SU_{a,k}(t))_{k\in\mathcal{K}_a}]^{\mathrm{T}}$ and $SD_a(t) = [(SD_{a,k}(t))_{k\in\mathcal{K}_a}]^{\mathrm{T}}$, respectively, over the scheduling horizon $\mathcal{T}$, as follows:[2]

$$\min_{\Omega} \sum_{a\in\mathcal{A}} \int_{\mathcal{T}} \big(C_a(G_a(t)) + 1_{K_a}^{\mathrm{T}} \big(SU_a(t) + SD_a(t)\big)\big)\, dt, \tag{1a}$$

$$\text{s.t. } B_a\theta_a(t) + M_a^{\mathrm{tie}} T_a(t) = M_a^{\mathrm{g}} G_a(t) - D_a(t) + M_a^{\mathrm{es}}\big(G_a^{\mathrm{es}}(t) - D_a^{\mathrm{es}}(t)\big), \quad \forall\, a\in\mathcal{A},\ t\in\mathcal{T}, \tag{1b}$$

$$\underline{G}_a I_a(t) \le G_a(t) \le \overline{G}_a I_a(t), \quad \forall\, a\in\mathcal{A},\ t\in\mathcal{T}, \tag{1c}$$

$$\underline{\dot{G}}_a^{SD} \int_{t-\epsilon}^{t+\epsilon} \dot{I}_a(t)dt \le \dot{G}_a(t) \le \overline{\dot{G}}_a^{SU} \int_{t-\epsilon}^{t+\epsilon} \dot{I}_a(t)dt, \ \forall\, a\in\mathcal{A}, t\in\mathcal{T}, \tag{1d}$$

[2]Note that 1_X and 0_X denote the X-dimensional vectors of ones and zeros, respectively. Unless otherwise specified, we make use of underline (overline) to represent the minimum (maximum) limit of the corresponding variable.

$$\int_{t}^{t+UT_a} I_a(t)dt \geq \mathrm{Diag}(UT_a) \int_{t-\epsilon}^{t+\epsilon} \dot{I}_a(t)dt, \quad \forall\, a \in \mathcal{A},\ t \in \mathcal{T}, \tag{1e}$$

$$\int_{t}^{t+DT_a} \big(1_{K_a} - I_a(t)\big)dt \geq \mathrm{Diag}(DT_a) \int_{t-\epsilon}^{t+\epsilon} -\dot{I}_a(t)dt, \quad \forall\, a \in \mathcal{A},\ t \in \mathcal{T}, \tag{1f}$$

$$SU_a(t) \geq V_a \int_{t-\epsilon}^{t+\epsilon} \dot{I}_a(t)dt, \qquad \forall\, a \in \mathcal{A},\ t \in \mathcal{T}, \tag{1g}$$

$$SD_a(t) \geq W_a \int_{t-\epsilon}^{t+\epsilon} -\dot{I}_a(t)dt, \quad \forall\, a \in \mathcal{A},\ t \in \mathcal{T}, \tag{1h}$$

$$\dot{E}_a^{\mathrm{es}}(t) = \eta^{\mathrm{c}} D_a^{\mathrm{es}}(t) - \eta^{\mathrm{d}^{-1}} G_a^{\mathrm{es}}(t), \forall\, a \in \mathcal{A},\ t \in \mathcal{T}, \tag{1i}$$

$$0_{R_a} \leq D_a^{\mathrm{es}}(t) \leq \overline{D}_a^{\mathrm{es}}, \qquad \forall\, a \in \mathcal{A},\ t \in \mathcal{T}, \tag{1j}$$

$$0_{R_a} \leq G_a^{\mathrm{es}}(t) \leq \overline{G}_a^{\mathrm{es}}, \qquad \forall\, a \in \mathcal{A},\ t \in \mathcal{T}, \tag{1k}$$

$$\underline{\dot{D}}_a^{\mathrm{es}} \leq \dot{D}_a^{\mathrm{es}}(t) \leq \overline{\dot{D}}_a^{\mathrm{es}}, \qquad \forall\, a \in \mathcal{A},\ t \in \mathcal{T}, \tag{1l}$$

$$\underline{\dot{G}}_a^{\mathrm{es}} \leq \dot{G}_a^{\mathrm{es}}(t) \leq \overline{\dot{G}}_a^{\mathrm{es}}, \qquad \forall\, a \in \mathcal{A},\ t \in \mathcal{T}, \tag{1m}$$

$$\underline{E}_a^{\mathrm{es}} \leq E_a^{\mathrm{es}}(t) \leq \overline{E}_a^{\mathrm{es}}, \qquad \forall\, a \in \mathcal{A},\ t \in \mathcal{T}, \tag{1n}$$

$$F_{a,(i,j)}(t) = \frac{\theta_{a,i}(t) - \theta_{a,j}(t)}{x_{a,(i,j)}}, \quad \forall\, a \in \mathcal{A}, \quad \forall\, (i,j) \in \mathcal{L}_a,\ t \in \mathcal{T}, \tag{1o}$$

$$T_{a,(i,j)}(t) = \frac{\theta_{a,i}(t) - \theta_{\mathring{a},j}(t)}{x^{\mathrm{tie}}_{a,(i,j)}}, \quad \forall\, a \in \mathcal{A}, \quad \forall\, (i,j) \in \mathcal{L}_a^{\mathrm{tie}},\ t \in \mathcal{T}, \tag{1p}$$

$$-\overline{F}_a \leq F_a(t) \leq \overline{F}_a, \qquad \forall\, a \in \mathcal{A},\ t \in \mathcal{T}, \tag{1q}$$

$$-\overline{T}_a \leq T_a(t) \leq \overline{T}_a, \qquad \forall\, a \in \mathcal{A},\ t \in \mathcal{T}, \tag{1r}$$

$$\theta_{1,1}(t) = 0, \qquad t \in \mathcal{T}, \tag{1s}$$

$$E_a^{\mathrm{es}}(0) = E_a^{\mathrm{es},0}, \qquad \forall\, a \in \mathcal{A},\ t \in \mathcal{T}, \tag{1t}$$

$$SU_a(t), SD_a(t) \geq 0_{K_a} \qquad \forall\, a \in \mathcal{A},\ t \in \mathcal{T}, \tag{1u}$$

in which $\Omega = \{G_a(t), I_a(t), SU_a(t), SD_a(t), G_a^{\mathrm{es}}(t), D_a^{\mathrm{es}}(t), E_a^{\mathrm{es}}(t), \theta_a(t), F_a(t), T_a(t)\}_{t\in\mathcal{T}, a\in\mathcal{A}}$ comprises the decision trajectories. The nodal power balance is enforced in (1b), where M_a^{tie}, M_a^{g}, and M_a^{es} respectively denote mapping matrices relating tielines, generating units, and ES de-

vices located in area a to corresponding buses. The power generation and ramping of units are constrained through (1c) and (1d), where diagonal matrices $\underline{G}_a$ ($\underline{\dot{G}}_a$) and $\overline{G}_a$ ($\overline{\dot{G}}_a$) refer respectively to minimum and maximum generation (ramping) limits, diagonal matrices $\overline{\dot{G}}_a^{SU}$ and $\overline{\dot{G}}_a^{SD}$ respectively represent the maximum startup and shutdown ramps, and the vector $\dot{I}_a(t) = [(\dot{I}_{a,k}(t))_{k\in\mathcal{K}_a}]^{\mathrm{T}}$ represents the time-derivatives of commitment status variables that embed impulse functions at ON/OFF time instants thus characterizing startup/shutdown through integration over a ϵ-neighborhood of those time instants. The minimum up and down times of units are imposed via (1e) and (1f), respectively, where vectors UT_a and DT_a respectively contain the minimum up and down times of units. Evaluated in (1g) and (1h) are respectively startup and shutdown costs, where diagonal matrices V_a and W_a respectively represent the unit startup and shutdown costs. The ES energy state equation is formulated in (1i) where η^{c} and η^{d} are diagonal matrices of charging and discharging efficiencies, respectively. The charging and discharging power (ramping) of ES devices are confined to their limits through (1j)–(1k) ((1l)–(1m)) and their energy limits are enforced in (1n). Transmission line and tieline power flows calculated in (1o)–(1p) are constrained to their respective limits in (1q)–(1r) where $x_{a,(i,j)}$ and $x^{\mathrm{tie}}_{a,(i,j)}$ represent the pertinent line reactance values. Without loss of generality, we set the voltage phase angle of bus 1 in area 1 to be zero as the system angle reference in (1s). The ES stored energy trajectories are initialized at $E_a^{\mathrm{es},0}$ in (1t) and the startup and shutdown costs are forced to take positive values through (1u). Finally, it is worth noting that the separation of variables and constraints into their respective areas in (1) facilitates the decomposition needed for the proposed distributed solution later.

3. Proposed Solution Methodology

3.1. Problem Statement

The continuous-time modeling of the multi-area UC problem in (1) leads to an infinite-dimensional decision space and renders it a computationally intractable optimization problem. In addition, the underlying assumption that areas disclose full information regarding local generation, load, and transmission network with a central operator may be difficult to satisfy in practice due to privacy concerns. Addressing these challenges calls for a computationally efficient privacy-preserving solution approach that i) enables projecting

the infinite-dimensional decision space of the problem in (1) into a finite-dimensional decision space with customized accuracy, and ii) determines the optimal generator and ES dispatch, as well as the interconnection power exchange, with limited information exchange. Next, we propose Bernstein function space for dimensionality reduction of the problem in (1) and deploy an ATC algorithm to solve the resulting finite-dimensional MILP problem.

3.2. Function Space Representation

We adopt the methodology in [18, 19] and project the continuous-time decision variables and parameters into a Bernstein function space of degree $Q = 3$, spanned by a set of polynomial basis functions defined as

$$b_q^{(Q)}(t) = \begin{pmatrix} Q \\ q \end{pmatrix} t^q (1-t)^{Q-q}, \\ t \in [0,1), q \in \mathcal{Q} = \{0, 1, \ldots, Q\}, \tag{2}$$

through which the continuous-time UC problem in (1) converts to a traditional optimization problem of finite dimension with Bernstein coefficients as decision variables.

Subdivide the scheduling horizon $\mathcal{T}$ into S nonoverlapping intervals $\mathcal{T}_s = [t_s, t_{s+1}), \rightarrow \mathcal{T} = \cup_{s=0}^{S-1} \mathcal{T}_s$ of equal length Δ, and construct for each interval s a set of shifted and scaled basis functions as follows:

$$b_{q,s}^{(Q),\mathrm{sh}}(t) = b_q^{(Q)} \left(\frac{t - t_s}{\Delta} \right), \ q \in \mathcal{Q}, \ t \in [t_s, t_{s+1}). \tag{3}$$

Now concatenate the interval basis functions in (3) to form a single vector $e^{(Q)}(t) = [(b_{q,s}^{(Q),\mathrm{sh}}(t))_{s \in \{0,\ldots,S-1\}, q \in \mathcal{Q}}]^{\mathrm{T}}$ spanning the entire scheduling horizon and including $P = S(Q+1)$ components. It will be useful to also collect the interval indices in set $s \in \mathcal{S} = \{0, \ldots, S-1\}$.

With these basic functions defined, we now outline the Bernstein function space representation of various components of the continuous-time UC problem in (1).

3.2.1. Generating Units

Power generation trajectories projected into the Bernstein function space spanned by $e^{(Q)}(t)$ are expressed as

$$G_a(t) = \widehat{G}_a e^{(Q)}(t), \ \forall\, a \in \mathcal{A}, \ t \in \mathcal{T}, \tag{4}$$

where $\widehat{G}_a$ is a $K_a \times P$ matrix of Bernstein coefficients. Generation ramping trajectories are then given by [36, 37]

$$\dot{G}_a(t) = \widehat{G}_a \dot{e}^{(Q)}(t) = \widehat{G}_a \left(M^{\text{der}} e^{(Q-1)}(t) \right) \tag{5}$$

$$= \widehat{\dot{G}}_a e^{(Q-1)}(t), \ \forall\, a \in \mathcal{A}, \ t \in \mathcal{T}, \tag{6}$$

where M^{der} is the $P \times (P-S)$ matrix relating the time-derivatives of Bernstein basis functions of degree Q to basis functions of degree $Q-1$ and

$$\widehat{\dot{G}}_a = \widehat{G}_a M^{\text{der}}, \ \forall\, a \in \mathcal{A}. \tag{7}$$

Let the binary variable trajectories $I_a(t)$ remain constant for each interval $\mathcal{T}_s \in \mathcal{T}$, as shown in Fig. 3. Denote the interval-specific binary variables by $I_a(t_s)_{s \in \mathcal{S}}$ and project the resultant trajectories in the function space spanned by $e^{(Q)}(t)$ as $I_a(t) = \widehat{I}_a e^{(Q)}(t), \ \forall\, a \in \mathcal{A}, \ t \in \mathcal{T}$, where $\widehat{I}_a$ is a $K_a \times P$ matrix of Bernstein coefficients. By enforcing the following conditions on Bernstein coefficients of commitment status trajectories of generator k in area a

$$\widehat{I}_{a,k,(Q+1)s+q} = \begin{cases} I_{a,k}(t_s), \ q \in \{0, \ldots, Q-2\}, \\ I_{a,k}(t_{s+1}), \ q \in \{Q-1, Q\}, \end{cases} \tag{8}$$

we guarantee that the approximate trajectory follows a smooth transition between intervals as shown by the solid black trace in Fig. 3. This then facilitates imposing the generation limits in the function space as

$$\underline{G}_a \widehat{I}_a \leq \widehat{G}_a \leq \overline{G}_a \widehat{I}_a, \ \forall\, a \in \mathcal{A}, \ t \in \mathcal{T}. \tag{9}$$

The startup and shutdown costs in each time interval $\mathcal{T}_s$, excluding the first interval, are denoted respectively by $SU_a(t_s)_{s \in \mathcal{S} \setminus \{0\}}$ and $SD_a(t_s)_{s \in \mathcal{S} \setminus \{0\}}$ and calculated as

$$SU_a(t_s) \geq V_a \left(I_a(t_s) - I_a(t_{s-1}) \right), \ \forall\, a \in \mathcal{A}, s \in \mathcal{S} \setminus \{0\}, \tag{10}$$

$$SD_a(t_s) \geq W_a \left(I_a(t_{s-1}) - I_a(t_s) \right), \forall\, a \in \mathcal{A}, s \in \mathcal{S} \setminus \{0\}, \tag{11}$$

$$SU_a(t_s), SD_a(t_s) \geq 0_{K_a}, \qquad \forall\, a \in \mathcal{A}, s \in \mathcal{S} \setminus \{0\}. \tag{12}$$

We refer interested readers to [18] for details on modeling minimum up and down time constraints and ramping constraints.

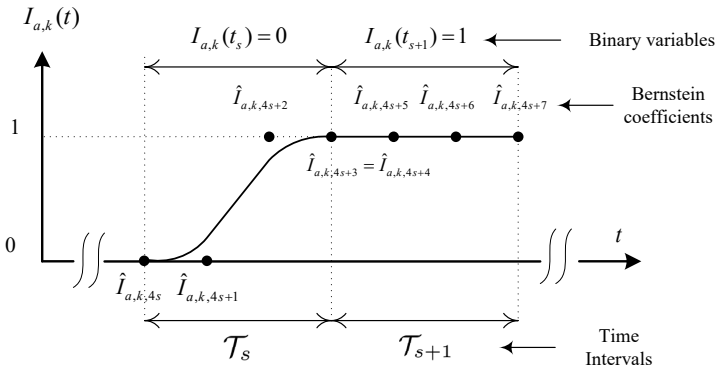

Figure 3: Illustrating consecutive intervals $\mathcal{T}_s$ and $\mathcal{T}_{s+1}$ with $Q = 3$ and binary variable trajectory $I_{a,k}(t)$ being 0 in $\mathcal{T}_s$ and 1 in $\mathcal{T}_{s+1}$. Filled black dots represent the Bernstein coefficients and the solid black trace indicates function space approximation of the commitment status trajectory that switches smoothly from OFF to ON state.

3.2.2. ES Devices

The ES charging and discharging power trajectories are projected into function space as $D_a^{\text{es}}(t) = \widehat{D}_a^{\text{es}} e^Q(t), G_a^{\text{es}}(t) = \widehat{G}_a^{\text{es}} e^Q(t), \forall\, a \in \mathcal{A}, t \in \mathcal{T}$, where $\widehat{D}_a^{\text{es}}$ and $\widehat{G}_a^{\text{es}}$ represent $R_a \times P$ matrices of Bernstein coefficients constrained to their limits as follows:

$$0_{K_a} 1_P^{\text{T}} \leq \widehat{D}_a^{\text{es}} \leq \overline{D}_a^{\text{es}} 1_P^{\text{T}},\ \forall\, a \in \mathcal{A}, \tag{13}$$

$$0_{K_a} 1_P^{\text{T}} \leq \widehat{G}_a^{\text{es}} \leq \overline{G}_a^{\text{es}} 1_P^{\text{T}},\ \forall\, a \in \mathcal{A}. \tag{14}$$

Similar to generating units, the charge and discharge ramping trajectories are then modeled as

$$\widehat{\dot{D}}_a^{\text{es}} = \widehat{D}_a^{\text{es}} M^{\text{der}},\ \widehat{\dot{G}}_a^{\text{es}} = \widehat{G}_a^{\text{es}} M^{\text{der}},\ \forall\, a \in \mathcal{A}, \tag{15}$$

where $\widehat{\dot{D}}_a^{\text{es}}$ and $\widehat{\dot{G}}_a^{\text{es}}$ are the $R_a \times (P - S)$ matrices of Bernstein coefficients that are constrained by

$$\underline{\dot{D}}_a^{\text{es}} 1_P^{\text{T}} \leq \widehat{\dot{D}}_a^{\text{es}} \leq \overline{\dot{D}}_a^{\text{es}} 1_P^{\text{T}},\ \forall\, a \in \mathcal{A}, \tag{16}$$

$$\underline{\dot{G}}_a^{\text{es}} 1_P^{\text{T}} \leq \widehat{\dot{G}}_a^{\text{es}} \leq \overline{\dot{G}}_a^{\text{es}} 1_P^{\text{T}},\ \forall\, a \in \mathcal{A}. \tag{17}$$

In order to model the ES energy trajectories, we integrate the energy state equation in (1i) and recast the resultant as

$$E_a^{\text{es}}(t) = E_a^{\text{es},0} + \left(\eta^{\text{c}} \widehat{D}_a^{\text{es}} - \eta^{\text{d}^{-1}} \widehat{G}_a^{\text{es}}\right) \int_0^t e^{(Q)}(t)\, dt$$

$$= E_a^{\mathrm{es},0} + \left(\eta^{\mathrm{c}}\widehat{D}_a^{\mathrm{es}} - \eta^{\mathrm{d}^{-1}}\widehat{G}_a^{\mathrm{es}}\right) M^{\mathrm{int}} e^{(Q+1)}(t)$$
$$= \widehat{E}_a^{\mathrm{es}} e^{(Q+1)}(t), \qquad \forall\, a \in \mathcal{A},\ t \in \mathcal{T},$$

where the $P \times (P+S)$ matrix M^{int} relates the integrals of Bernstein basis functions of degree Q to basis functions of degree $Q+1$ [36, 37], and $\widehat{E}_a^{\mathrm{es}}$ represents the $R_a \times (P+S)$ matrix of Bernstein coefficients defined as

$$\widehat{E}_a^{\mathrm{es}} = E_a^{\mathrm{es},0} 1_{(P+S)}^{\mathrm{T}} + \left(\eta^{\mathrm{c}}\widehat{D}_a^{\mathrm{es}} - \eta^{\mathrm{d}^{-1}}\widehat{G}_a^{\mathrm{es}}\right) M^{\mathrm{int}}, \forall\, a \in \mathcal{A}, \tag{18}$$

and constrained by

$$\underline{E}_a^{\mathrm{es}} 1_{(P+S)}^{\mathrm{T}} \leq \widehat{E}_a^{\mathrm{es}} \leq \overline{E}_a^{\mathrm{es}} 1_{(P+S)}^{\mathrm{T}},\ \forall\, a \in \mathcal{A}. \tag{19}$$

3.2.3. Network Constraints

Project voltage phase angles and line and tieline power flow trajectories into function space as $\theta_a(t) = \widehat{\theta}_a e^Q(t)$, $F_a(t) = \widehat{F}_a e^Q(t)$, and $T_a(t) = \widehat{T}_a e^Q(t)$, respectively, $\forall\, a \in \mathcal{A},\ t \in \mathcal{T}$. The flows are constrained by

$$-\overline{F}_a 1_P^{\mathrm{T}} \leq \widehat{F}_a \leq \overline{F}_a 1_P^{\mathrm{T}},\ \forall\, a \in \mathcal{A}, \tag{20}$$
$$-\overline{T}_a 1_P^{\mathrm{T}} \leq \widehat{T}_a \leq \overline{T}_a 1_P^{\mathrm{T}},\ \forall\, a \in \mathcal{A}, \tag{21}$$

where $\widehat{\theta}_a$, $\widehat{F}_a$, and $\widehat{T}_a$ are respectively $N_a \times P$, $|\mathcal{L}_a| \times P$, and $|\mathcal{L}_a^{\mathrm{tie}}| \times P$ matrices of Bernstein coefficients. With $\widehat{\theta}_a$, $\widehat{F}_a$, and $\widehat{T}_a$ in place, it is also straightforward to recast (1o) and (1p) as

$$\widehat{F}_{a,(i,j)} = \frac{\widehat{\theta}_{a,i} - \widehat{\theta}_{a,j}}{x_{a,(i,j)}},\quad \forall\, a \in \mathcal{A},\ (i,j) \in \mathcal{L}_a, \tag{22}$$

$$\widehat{T}_{a,(i,j)} = \frac{\widehat{\theta}_{a,i} - \widehat{\theta}_{a',j}}{x^{\mathrm{tie}}_{a,(i,j)}},\quad \forall\, a \in \mathcal{A},\ (i,j) \in \mathcal{L}_a^{\mathrm{tie}}, \tag{23}$$

respectively, where $\widehat{\theta}_{a,i}$ and $\widehat{\theta}_{a,j}$ respectively refer to the i^{th} and j^{th} rows of $\widehat{\theta}_a$, and (i,j) refers to the pertinent row in $\widehat{F}_a$ and $\widehat{T}_a$. Further, to enforce the zero voltage phase angle of the reference bus over the scheduling horizon, the associated Bernstein coefficients are all set to zero as

$$\widehat{\theta}_{1,1}^{\mathrm{T}} = 0_P. \tag{24}$$

Finally, by substituting the voltage phase angle, generation, and tieline power trajectories with their function space representation, and denoting the nodal

load Bernstein coefficients with the $N_a \times P$ matrix $\widehat{D}_a$, the nodal power balance constraint in (1b) can be expressed as

$$B_a\widehat{\theta}_a + M_a^{\text{tie}}\widehat{T}_a = M_a^{\text{g}}\widehat{G}_a - \widehat{D}_a,\ \forall\, a \in \mathcal{A}. \tag{25}$$

3.2.4. Objective Function

We approximate the convex cost function $C_{a,k}(G_{a,k}(t))$ of generator $k \in \mathcal{K}_a$ with a piece-wise linear function of $H_{a,k}$ segments. To each segment $h \in \{1, \ldots, H_{a,k}\}$ we ascribe a positive-valued auxiliary variable trajectory $g_{a,k,h}(t)$ and the segment length $\overline{g}_{a,k,h}$ and collect the h^{th} auxiliary variables attributed to generators located in area a in vector $g_{a,h}(t) = [(g_{a,k,h}(t))_{k\in\mathcal{K}_a}]^{\text{T}}$ and the segment lengths in vector $\overline{g}_{a,h}$ therein. By substituting the continuous-time trajectories with the pertinent function space approximations and leveraging the integral property of Bernstein polynomials [36, 37], the objective function in (1a) is recast as follows

$$\begin{aligned}\mathcal{J}_a = &\sum_{s\in\mathcal{S}\setminus\{0\}} 1_{K_a}^{\text{T}}\left(SU_a(t_s) + SD_a(t_s)\right)\\ &+ \Delta\sum_{s\in\mathcal{S}}\sum_{k\in\mathcal{K}_a} I_{a,k}(t_s)C_{a,k}(\underline{G}_{a,k})\\ &+ \Delta\frac{\sum_{h=1}^{H_{a,k}} 1_{K_a}^{\text{T}}\gamma_{a,h}\widehat{g}_{a,h}1_P}{Q+1},\end{aligned} \tag{26}$$

where $\gamma_{a,h}$ represents the $K_a \times K_a$ diagonal matrix containing the slope of the secant connecting the two endpoints of linear cost function approximation, and $\widehat{g}_{a,h}$ represents the $K_a \times P$ matrix of Bernstein coefficients attributed to auxiliary variables, i.e., $g_{a,h}(t) = \widehat{g}_{a,h}e^{(Q)}(t),\ \forall\, a \in \mathcal{A},\ h \in \mathcal{H}_{a,k},\ t \in \mathcal{T}$. The function space coefficients of generation trajectories relate to that of auxiliary variables and commitment statuses as

$$\widehat{G}_a = \underline{G}_a\widehat{I}_a + \sum_{h=1}^{H_{a,k}}\widehat{g}_{a,h}, \tag{27}$$

and $\widehat{g}_{a,h}$ is subject to the following box constraint:

$$0_{K_a}1_P^{\text{T}} \le \widehat{g}_{a,h} \le \overline{g}_{a,h}1_P^{\text{T}}. \tag{28}$$

3.2.5. Centralized Unit Commitment Problem

Given the function space representation of operational constraints furnished above, the continuous-time UC problem in (1) is converted to the following traditional optimization problem:

$$\min_{\widehat{\Omega}} \sum_{a\in\mathcal{A}} \mathcal{J}_a \tag{29a}$$

$$\text{s.t. Constraints (7)–(28)}, \tag{29b}$$

$$\text{Generation Ramping Constraints}, \tag{29c}$$

$$\text{Minimum Up/Down Time Constraints}, \tag{29d}$$

$$\text{Continuity Constraints}, \tag{29e}$$

optimizing over the set of decision variables $\widehat{\Omega} = \widehat{\Omega}_1 \cup \widehat{\Omega}_2$, where $\widehat{\Omega}_1 = \{\widehat{G}_a, \widehat{I}_a, \widehat{G}^{\text{es}}_a, \widehat{D}^{\text{es}}_a, \widehat{E}^{\text{es}}_a, \widehat{\theta}_a, \widehat{F}_a, \widehat{T}_a\}_{a\in\mathcal{A}}$ and $\widehat{\Omega}_2 = \{I_a(t_s), SU_a(t_s), SD_a(t_s)\}_{a\in\mathcal{A},s\in\mathcal{S}}$. We refer interested readers to [18, 19] for details on continuity constraints that enable smooth transition of optimal decision trajectories between intervals $\mathcal{T}_s$ and $\mathcal{T}_{s+1}$.

3.3. Distributed Solution for Continuous-time UC Problem

We employ an ATC algorithm (see, e.g., [38]) to solve the centralized multi-area UC problem projected into Bernstein function space in (29) in an iterative and distributed manner. The solution algorithm is conceptualized as hierarchical coordination of a two-level optimization problem where the lower and upper levels consist of per-area UC sub-problems and a central coordinator problem, respectively. The coordination is enabled by identifying shared variables among areas (i.e., boundary-bus voltage phase angles) and corresponding duplicate variables (i.e., copy of those shared variables as seen by adjacent areas) to them, enforcing consensus constraints to equate the shared and duplicate variables via augmented Lagrangian approach, and obtaining the optimal penalty multipliers as well as duplicate variables through iterative data exchange between upper- and lower-level problems (see Fig. 4 for a visual illustration). A detailed account of the ATC algorithm is presented next.

Define $\mathcal{B}_a$ as the set of boundary buses in area $a \in \mathcal{A}$ and associate a P-dimensional row vector of duplicate variables $\widehat{\psi}_{a,i}$ to each bus $i \in \mathcal{B}_a$. Likewise, $\widehat{\psi}_{a',i}$ represent the duplicate variables for the shared variable $\widehat{\theta}_{a',j}$, which is a copy of boundary bus voltage angle of adjacent area. For $(i,j) \in$

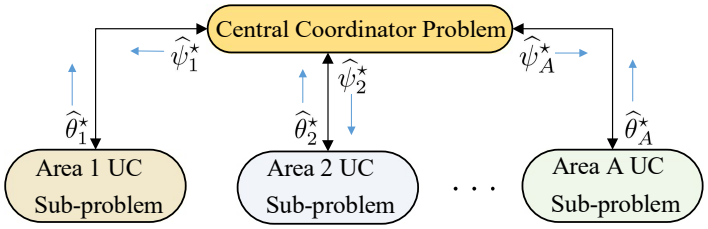

Figure 4: Hierarchical structure of an ATC algorithm where per-area UC sub-problems (31) are solved at each iteration of the algorithm and the optimal shared variables, $\widehat{\theta}^\star, a \in \mathcal{A}$, are communicated to the central coordinator, which then solves the problem in (32) and returns the optimal duplicate variables $\widehat{\psi}^\star, a \in \mathcal{A}$, to each area.

$\mathcal{L}_a^{\text{tie}}$, the consistency constraints equate the Bernstein coefficients of voltage phase angles and the corresponding duplicate variables as

$$\widehat{\theta}_{a,i} = \widehat{\psi}_{a,i},\ \widehat{\theta}_{a',j} = \widehat{\psi}_{a',j},\ \forall\, a, a' \in \mathcal{A},\ (i,j) \in \mathcal{L}^{\text{tie}}. \tag{30}$$

The solution algorithm is implemented through the following three steps.

3.3.1. Solving Per-area UC Sub-problem (Step 1)

Each area solves the following UC sub-problem with augmented objective function at each iteration z

$$\begin{aligned}
\min_{\widehat{\theta}_{a,i}^{(z)}, \widehat{\theta}_{a',j}^{(z)}}\ & \mathcal{J}_a^{(z)} + \sum_{(i,j)\in\mathcal{L}_a^{\text{tie}}} \big(\widehat{\psi}_{a,i}^{\star(z-1)} - \widehat{\theta}_{a,i}^{(z)}\big)\lambda_{a,i}^{\star(z-1)} \\
& + \|\big(\widehat{\psi}_{a,i}^{\star(z-1)} - \widehat{\theta}_{a,i}^{(z)}\big)\rho_{a,i}^{\star(z-1)}\|_2^2 \\
& + \big(\widehat{\psi}_{a',j}^{\star(z-1)} - \widehat{\theta}_{a',j}^{(z)}\big)\lambda_{a',j}^{\star(z-1)} \\
& + \|\big(\widehat{\psi}_{a',j}^{\star(z-1)} - \widehat{\theta}_{a',j}^{(z)}\big)\rho_{a',j}^{\star(z-1)}\|_2^2 && \text{(31a)} \\
\text{s.t. } & \text{Constraints } [(7)\text{–}(28)]_a, && \text{(31b)} \\
& [\text{Generation Ramping Constraints}]_a, && \text{(31c)} \\
& [\text{Minimum Up/Down Time Constraints}]_a, && \text{(31d)} \\
& [\text{Continuity Constraints}]_a, && \text{(31e)}
\end{aligned}$$

where $\widehat{\psi}_{a,i}^{\star(z-1)}$ and $\widehat{\psi}_{a',j}^{\star(z-1)}$ are optimal duplicate variables calculated in Step 2 of iteration $z-1$, and $\lambda_{a,i}^{\star(z-1)}$, $\lambda_{a',j}^{\star(z-1)}$, $\rho_{a,i}^{\star(z-1)}$ and $\rho_{a',j}^{\star(z-1)}$ are P-dimensional vectors of penalty multipliers updated in Step 3 of the iteration $z-1$.

The consistency constraints are enforced by forming the augmented Lagrangian in (31a), and $[\cdot]_a$ indicates the subset of constraints pertinent to area a. We note that, unlike the centralized UC problem in (29), which is an MILP, the per-area sub-problem in (31) is a mixed-integer quadratic programming (MIQP) problem.

3.3.2. Optimizing Duplicate Variables (Step 2)

Each area obtains the optimal Bernstein coefficients $\widehat{\theta}^{\star(z)}_{a,i}$ and $\widehat{\theta}^{\star(z)}_{a',j}$ from the solution of (31) in Step 1 and sends them to the coordinator, which then calculates the optimal duplicate variables through the solution of the following unconstrained optimization problem:

$$\begin{aligned}\min_{\widehat{\psi}^{(z)}_{a,i},\widehat{\psi}^{(z)}_{a',j}} \sum_{a\in\mathcal{A}} \sum_{(i,j)\in\mathcal{L}^{\text{tie}}_a} & \big(\widehat{\psi}^{(z)}_{a,i} - \widehat{\theta}^{\star(z)}_{a,i}\big)\lambda^{\star(z-1)}_{a,i} \\ & + \|\big(\widehat{\psi}^{(z)}_{a,i} - \widehat{\theta}^{\star(z)}_{a,i}\big)\rho^{\star(z-1)}_{a,i}\|_2^2 + \big(\widehat{\psi}^{(z)}_{a',j} - \widehat{\theta}^{\star(z)}_{a',j}\big)\lambda^{\star(\text{z}-1)}_{a',j} \\ & + \|\big(\widehat{\psi}^{(z)}_{a',j} - \widehat{\theta}^{\star(z)}_{a',j}\big)\rho^{\star(z-1)}_{a',j}\|_2^2, \end{aligned} \tag{32}$$

where $\widehat{\theta}^{\star(z)}_{a,i}$ and $\widehat{\theta}^{\star(z)}_{a',j}$ are optimal voltage phase angle Bernstein coefficients calculated in Step 1 of iteration z.

3.3.3. Updating Penalty Multipliers (Step 3)

For $a \in \mathcal{A}$ and $(i,j) \in \mathcal{L}^{\text{tie}}_a$, penalty multipliers are updated as

$$\lambda^{\star(z)}_{a,i} = \lambda^{\star(z-1)}_{a,i} + 2\big(\rho^{\star(z-1)}_{a,i}\big)^{\circ 2} \odot \big(\widehat{\psi}^{\star(z)}_{a,i} - \widehat{\theta}^{\star(z)}_{a,i}\big), \tag{33}$$

$$\lambda^{\star(z)}_{a',j} = \lambda^{\star(z-1)}_{a',j} + 2\big(\rho^{\star(z-1)}_{a',j}\big)^{\circ 2} \odot \big(\widehat{\psi}^{\star(z)}_{a',j} - \widehat{\theta}^{\star(z)}_{a',j}\big), \tag{34}$$

$$\rho^{\star(z)}_{a,i} = \alpha\rho^{\star(z-1)}_{a,i}, \quad \rho^{\star(z)}_{a',j} = \alpha\rho^{\star(z-1)}_{a',j}, \tag{35}$$

where "$(\cdot)^{\circ 2}$" and "$\odot$" respectively indicate the component-wise square and product operators, and α is a the update coefficient which takes values greater than or equal to 1 [33] [38]. The iterative algorithm starts with the initialization of penalty multipliers and duplicate variables in step 1 and stops under the condition that

$$\begin{aligned}\text{abs}\big(\widehat{\psi}^{\star(z)}_{a,i} - \widehat{\theta}^{\star(z)}_{a,i}\big), \text{abs}\big(\widehat{\psi}^{\star(z)}_{a',j} - \widehat{\theta}^{\star(z)}_{a',j}\big) \le \epsilon 1_P, \\ \forall\, a \in \mathcal{A},\ \forall\, (i,j) \in \mathcal{L}^{\text{tie}}_a, \end{aligned} \tag{36}$$

where "abs" denotes the component-wise absolute value operator and ϵ represents a predetermined mismatch threshold. Since the relationship between

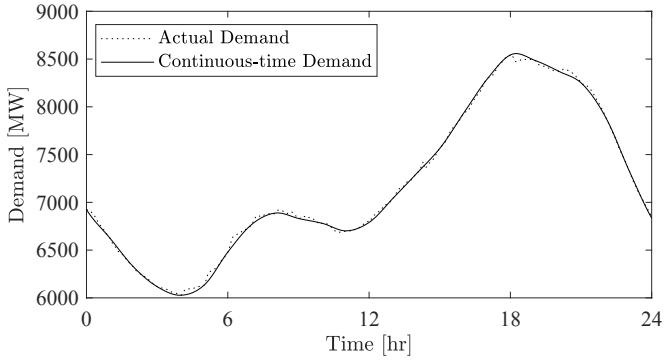

Figure 5: Continuous-time system demand for the three-area IEEE-RTS.

penalty multipliers and solution efficiency is more experiential than epistemic, determining the most efficient penalty multipliers in step 1 requires some trial and error to balance multiplier values with computational performance [38].

4. Numerical Case Studies

In this section, we provide details on simulation setting, introduce performance indices, and present the numerical results to demonstrate the effectiveness and performance of the proposed solution methodology.

4.1. Simulation Setting and Performance Indices

The proposed distributed solution approach for variational multi-area UC problem, presented in Section 3.3, is applied to the three-area IEEE-RTS [39] with 96 generating units, 73 buses, 115 transmission lines, and 5 tielines. The continuous-time trajectories are projected into a Bernstein function space, and span a scheduling horizon of $\mathcal{T} = [0, 24]$ [hr]. The Bernstein coefficients of system load trajectory is obtained from 5-minute real-time load data of California ISO (CAISO) for August 10, 2023 [40], scaled down to the three-area IEEE-RTS peak load of 8550 [MW] as shown in Fig. 5. The system load, in turn, is distributed over individual buses proportional to pertinent load factors provided in [39]. We adopt a cold-start approach within the ATC algorithm by initializing the optimal duplicate variables, $\widehat{\psi}^{\star(0)}_{a,i}$ and $\widehat{\psi}^{\star(0)}_{a',j}$, in (31) at 0s and set the mismatch threshold ϵ to be 0.006.

To examine the performance of distributed solution as compared to centralized counterpart, i.e., the solution of (29), the following *performance*

indices are defined and calculated:

$$\delta^{\text{cost}} = \frac{\sum_{a\in\mathcal{A}} \text{abs}\big(\mathcal{J}_a^\star - \mathcal{J}_a^{\star(Z)}\big)}{\sum_{a\in\mathcal{A}} \mathcal{J}_a^\star} \times 100\%, \tag{37}$$

$$\delta^{\text{gen}} = \frac{\sum_{a\in\mathcal{A}} \int_{t\in\mathcal{T}} \mathbb{1}_{K_a}^{\text{T}} \text{abs}\big(G_a^\star(t) - G_a^{\star(Z)}(t)\big)dt}{\sum_{a\in\mathcal{A}} \int_{t\in\mathcal{T}} D_a(t)dt} \times 100\%, \tag{38}$$

$$\delta^{\text{es}} = \Bigg(\frac{\sum_{a\in\mathcal{A}} \int_{t\in\mathcal{T}} \mathbb{1}_{R_a}^{\text{T}} \text{abs}\big(G_a^{\text{es}\star}(t) - G_a^{\text{es}\star(Z)}(t)\big)dt}{\sum_{a\in\mathcal{A}} \int_{t\in\mathcal{T}} D_a(t)dt} + \frac{\sum_{a\in\mathcal{A}} \int_{t\in\mathcal{T}} \mathbb{1}_{R_a}^{\text{T}} \text{abs}\big(D_a^{\text{es}\star}(t) - D_a^{\text{es}\star(Z)}(t)\big)dt}{\sum_{a\in\mathcal{A}} \int_{t\in\mathcal{T}} D_a(t)dt} \Bigg) \times 100\%, \tag{39}$$

$$\delta^{\text{RT}} = \int_{t\in\mathcal{T}} \big(\sum_{a\in\mathcal{A}} \mathbb{1}_{K_a}^{\text{T}} \text{abs} G_a^\star(t) - \sum_{a\in\mathcal{A}} D_a(t) \big) dt, \tag{40}$$

where Z is the minimum number of iterations needed to satisfy (36), and $\mathcal{J}_a^\star$ ($\mathcal{J}_a^{\star(Z)}$), $G_a^\star(t)$ ($G_a^{\star(Z)}(t)$), $D_a^{\text{es}\star}(t)$ ($D_a^{\text{es}\star(Z)}(t)$), and $G_a^{\text{es}\star}(t)$ ($G_a^{\text{es}\star(Z)}(t)$) are respectively the optimal per-area operation cost, generation dispatch, and charging and discharging power trajectories obtained from the centralized (distributed) solution. The index δ^{cost} represents the relative cost mismatch between distributed and benchmark centralized solutions, and δ^{gen} and δ^{es} indicate the total energy mismatch between distributed and centralized solutions relative to total energy demand of the three-area network over the scheduling horizon, respectively attributed to generating units and ES devices. For simplicity of exposition, we refer to the indices as *percentage relative errors*.

4.2. Simulation Results

We consider the following three cases involving the three-area IEEE-RTS: i) Case 1: with unaltered ramp limits, ii) Case 2: with reduced ramp limits, and iii) Case 3: Case 2 + energy storage. For all cases, we use the three-area IEEE-RTS network data available at [39], except we reduce the maximum power capacity limits of the tielines connecting buses 13 and 21 in area 1 respectively to bus 15 in area 2 and bus 25 in area 3 from 500 [MW] to 100 [MW]. This was done to enable potential congestion in tielines.

In Case 1, the penalty multipliers $\lambda_{a,i}^{(0)}, \lambda_{a',j}^{(0)}, \rho_{a,i}^{(0)}, \rho_{a',j}^{(0)}$ are initialized at 60 and the update coefficient α at 1.0 , as discussed in Section 3.3.3. The pro-

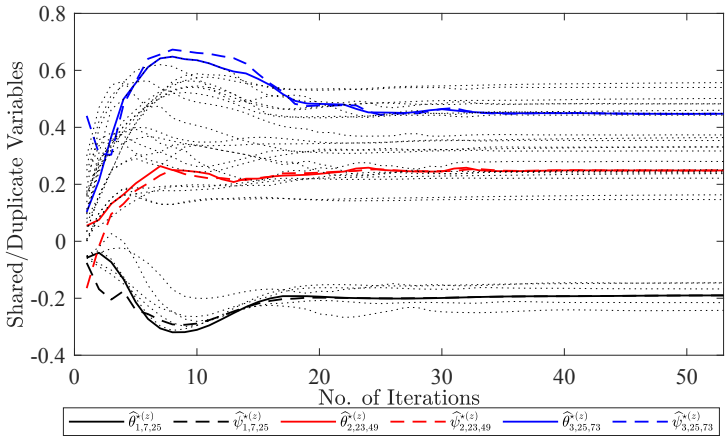

Figure 6: Convergence of the first Bernstein coefficient, $q = 0$, of shared (duplicate) variables attributed to time intervals $s = 6, 12, 18$ that correspond respectively to the 25^{th}, 49^{th}, and 73^{th} entries of vector $\widehat{\theta}^{\star(z)}_{a,i}$ ($\widehat{\psi}^{\star(z)}_{a,i}$) where $a \in \mathcal{A}$ and $i \in \mathcal{B}_a$. The three representative buses $i = 7, 23, 25$ in areas $a = 1, 2, 3$, respectively, are highlighted with black, red, and blue colors with solid (dashed) traces indicating the shared (duplicate) variable coefficients, while rest of variables are denoted by dotted gray traces.

gression of shared and duplicate variable Bernstein coefficients versus number of iterations is plotted in Fig. 6, where the three representative buses 7, 23, and 25 respectively in areas 1, 2, and 3 are distinguished with black, red, and blue colors with solid (dashed) traces indicating the shared (duplicate) variable coefficients, while the rest of variables are denoted by dotted gray traces. For the first 20 iteration, given that the consensus has not yet been established, the shared variable coefficients differ from that of duplicate counterparts. As the iterations progress, the shared variables coordinate with their respective duplicates to optimize the generated and imported/exported power in each area, eventually satisfying the maximum threshold mismatch condition (36) in 53 iterations and leading to optimal multi-area operation cost of \$1,468,544. The optimal decision trajectories obtained from distributed solution closely match those of centralized counterpart as confirmed by performance indices presented in Table 1, amounting to $\delta^{\text{cost}} = 0.108\%$ and $\delta^{\text{gen}} = 2.22\%$.

In Case 2, we synthesize an extreme condition of ramping capability shortage via scaling down the ramping limits of all generators located in area 1 by a factor of 3. Initialize the penalty multipliers $\lambda^{(0)}_{a,i}, \lambda^{(0)}_{a',j}, \rho^{(0)}_{a,i}, \rho^{(0)}_{a',j}$ at 55 and

Table 1: Performance Indices for Cases 1–3

Case	δ^{cost} [%]	δ^{gen} [%]	δ^{es} [%]
1	0.108	2.22	-
2	0.128	2.63	-
3	0.105	1.60	0.31

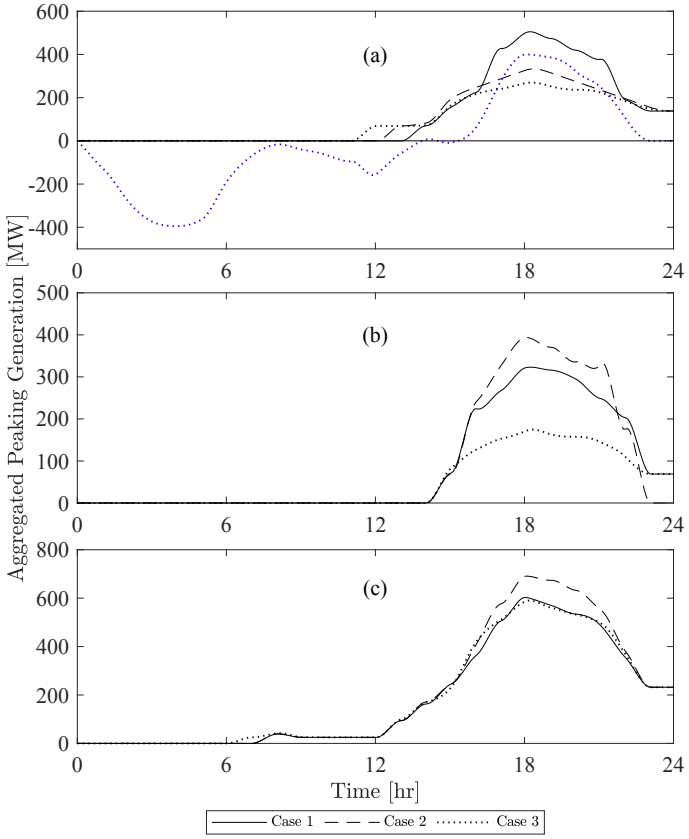

Figure 7: Aggregate peaking generation for areas (a) 1, (b) 2, and (c) 3, which are distinguished with black solid, dashed, and dotted traces for Cases 1–3, respectively. The blue trace represents the net power generated in Case 3 by the ES device in area 1 with negative and positive values referring respectively to charging and discharging powers.

the update coefficient α at 1.0. The distributed solution takes 39 iterations to satisfy (36), where the relative errors δ^{cost} and δ^{gen} respectively evaluate to 0.128% and 2.63% (see Table 1), highlighting the capability of distributed

solution to reach close vicinity of centralized solution. Despite the stricter ramping constraints imposed on generators in area 1, the optimal multi-area operating cost increases merely by \$872 due to contribution of fast-ramping resources in areas 2 and 3 in collaboratively supplying the load ramp requirement in area 1. This is confirmed by Figs. 7b and 7c where the aggregate peaking generation[3] in areas 2 and 3 increase in Case 2 (dashed black trace) as compared to Case 1 (solid black trace) to counterbalance the reduced peaking generation in area 1 in Case 2, as shown in Fig. 7a.

In Case 3, we build on Case 2 by adding a fast-ramping ES device of 400 [MW] charge and discharge power capacity, 2,000 [MWh] of energy capacity, 25 [MW/min] of ramping capability, and 90% of charge and discharge efficiency, to bus 20 in area 1. Sized roughly around the generation capacity of the largest unit in the three-area IEEE-RTS, this ES device mimics a utility-owned asset with no charging utility and discharging cost assigned (aligned with the objective function (1a) with ES utility/cost functions neglected[4]). Having initialized the penalty multipliers and the update coefficient at the same values as in Case 1, the distributed solution of Case 3 satisfies the threshold mismatch condition of (36) in 48 iterations with relative errors δ^{cost}, δ^{gen}, and δ^{es} evaluating respectively to 0.105%, 1.60%, and 0.31% as provided in Table 1. The operation cost in Case 3 reduces by \$11,080 as compared to Case 2 due to economic efficiency offered by the ES device via peak-demand supply and fast-ramping capability. More specifically, the ES device picks up a share of peak-demand not only in area 1 but also in areas 2 and 3, thus, substituting for the more expensive peaking generation resources plotted in Fig. 7 as the dotted black (blue) trace referring to aggregate peaking generation (ES device net power).

The power flow trajectory of the tieline connecting bus 21 in area 1 to bus 25 in area 3 is plotted in Fig. 8 for Cases 1–3. In Cases 1 and 2, the tieline is congested during $[1, 12]$ [hr] so that the maximum transferable power is exported from area 1 to area 3. In Case 1, as the load increases in $[12, 24]$ [hr], area 1 reduces the power export to area 3 to enable supplying the local peak demand. In Case 2, however, the power export from area 1 to area 3 reduces considerably to the extent that area 1 imports power during

[3]The aggregate peaking generation is defined as the sum of dispatched power from the relatively expensive units (U100 and U197) started up to supply peak demand.

[4]It is straightforward to incorporate ES charging utility and discharging cost functions in the objective function of (1a). Interested readers are referred to [19].

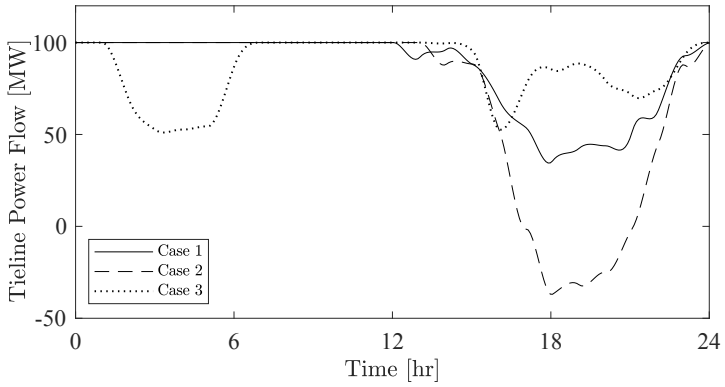

Figure 8: Power flow of the tieline connecting bus 21 in area 1 to bus 25 in area 3, for Cases 1–3.

Table 2: Computational Performance of Distributed Solution for three-area IEEE-RTS

Case	Number of Iterations	CPU Time [sec]
1	53	3,346
2	39	3,753
3	48	4,298

$[17, 21]$ [hr] to alleviate ramping capability shortage. In Case 3, the power export from area 1 to area 3 reduces during $[1, 6]$ [hr] to accommodate for local charging of ES device while the export increases considerably during peak-load hours as compared to Cases 1 and 2 due to ES discharging. The numerical results of Cases 3 highlights the ability for the proposed distributed solution to enable effective sharing of ES operational flexibility among areas.

4.3. Computational Performance and Comparisons

The proposed distributed solution approach is implemented in GAMS [41] and the computations are carried out on a desktop computer with a 3.70 [GHz] i9 CPU and 32 [GB] RAM, using CPLEX 12.10.0 solver [42] with the duality gap set at 0.01%. The CPU times and number of iterations to satisfy (36) are reported in Table 2 for all three cases, and Fig. 9 plots the changes in percentage relative cost error, δ^{cost}, as the iterations progress. For day-ahead scheduling, the proposed distributed approach provides a reasonably accurate solution, as measured by the indices in Table 1, within a practically adoptable CPU time of less than 1.2 hours for all cases. Notably, although the performance index δ^{cost} for cases 1–3 starts at a high value of

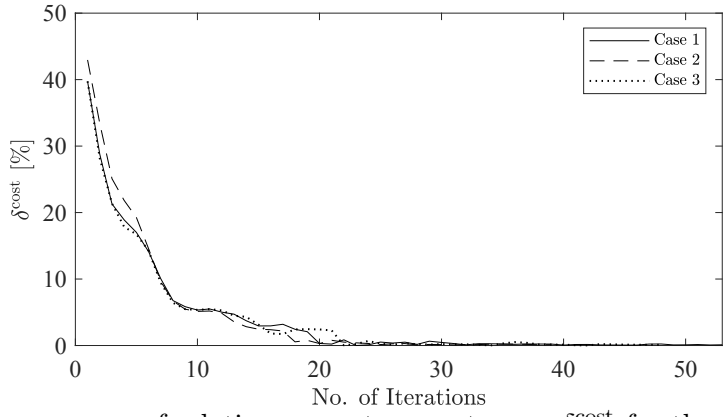

Figure 9: Convergence of relative percentage cost error δ^{cost} for three-area IEEE-RTS.

approximately 40%, it rapidly decreases to reasonably low values within the first 30 iterations.

4.3.1. Computational Scalability

To evaluate the computational scalability of the proposed algorithm, we extend its implementation to a larger 146-bus network comprising 6 areas and 13 tielines. This larger network is formed by mirroring the IEEE-RTS from Case 1 and connecting the two mirrored networks with 3 additional tielines, parameters for which are reported in Table 3. Initializing the penalty multipliers and the update coefficient at the same values as in Case 1, the distributed solution for this larger network meets the stopping criteria of (36) in 60 iterations with relative errors δ^{cost} of 0.11% and with operating cost of \$2,837,466. The performance of the algorithm for different values of update coefficients is illustrated in Fig. 10 and Table 4. Despite the greater numbers of buses, areas, and tielines, the proposed distributed algorithm demonstrates performance metrics that are very close to those of Case 1, showcasing its

Table 3: Parameters for Additional Tielines in Six-Area Mirrored IEEE-RTS

Tieline Number	Sending End (Area-Bus)	Receiving End (Area-Bus)	Reactance (pu)	Capacity (MW)
T11	1-6	1'-8	0.075	100
T12	2-2	2'-9	0.075	100
T13	3-1	3'-7	0.097	100

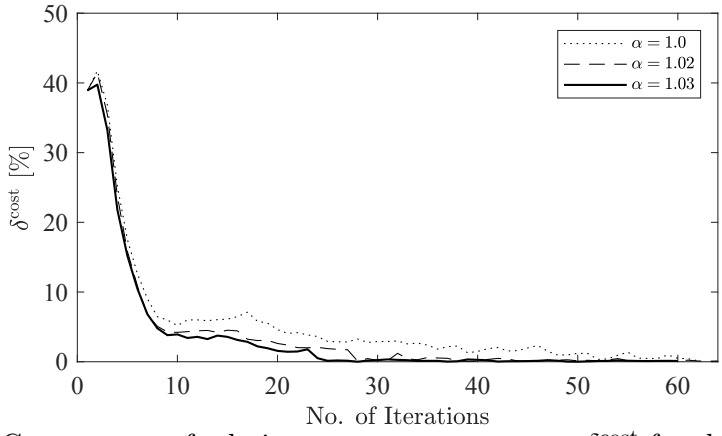

Figure 10: Convergence of relative percentage cost error δ^{cost} for the six-area mirrored IEEE-RTS with different values of update coefficient α.

Table 4: Computational Performance of Distributed Solution for the Six-Area Mirrored IEEE-RTS

α	Number of Iterations	CPU Time [Sec]	Operating Cost [$]	δ^{cost}
1.0	62	2,918	2,826,669	0.14
1.02	64	3,283	2,831,245	0.10
1.03	60	3,863	2,837,466	0.11

ability to scale to larger systems.

4.3.2. Comparison with Discrete-time Models

Using Bernstein basis functions in the proposed method enables near-optimal continuous-time trajectories that capture real-time load and generation variations while preserving the essence of hourly intervals. At the same time, a straightforward alternative to enhance solution granularity and better address real-time imbalances compared to current hourly-interval models is to reduce the scheduling interval in discrete-time formulations, but they significantly increase the overall problem size by introducing many more binary commitment variables [43].

Table 5 compares the number of binary and continuous variables for generating units in a 24-hour UC problem on IEEE-RTS using continuous- and discrete-time methodologies, highlighting the sharp increase in binary variables as the length of scheduling interval decreases. The use of distributed

Table 5: Total Numbers of Commitment Status (Binary) and Generation (Continuous) Variables in 24-hour UC problem for IEEE-RTS

UC Model	Commitment Status	Generation
Continuous-time (distributed)	768	3,072
Continuous-time (centralized)	2,304	9,216
Discrete-time (hourly intervals)	2,304	2,304
Discrete-time (quarter-hourly intervals)	9,216	9,216

Table 6: Comparing Performance Metrics of Different UC Models for IEEE-RTS

UC Model	CPU Time [Sec]	Operating Cost [$]	δ^{RT} [MW]
Continuous-time (distributed)	3,346	1,468,544	6,999
Continuous-time (centralized)	395	1,466,951	5,609
Discrete-time (hourly intervals)	21	1,469,504	6,183
Discrete-time (quarter-hourly intervals)	294	1,486,247	31,397

methodology further reduces the binary variables for each area's sub-problem (formulated as MIQP), yielding locally optimal solution within the duality gap, for each iteration. Likewise, since the coordinating problem solved at the central coordinator (i.e., the QCP) is convex, it guarantees a local optimal solution, leveraging the properties of the adopted distributed algorithm. Furthermore, due to convexity, any local solution to the linear optimization problem in functional space is also globally optimal. Solutions to linear optimization models in functional space can be efficiently approximated with available solvers (e.g., CPLEX, Gurobi). In contrast, discrete-time integer optimization is nonconvex, meaning a locally optimal solution may not be close to the global optimum. Moreover, discrete-time optimization models face scalability issues, as the combinatorial explosion in the search space significantly increases computation time.

Plotted in Fig. 11 are comparisons of the aggregate generation schedule obtained from three different solution methodologies with the real-time load profile presented in Fig. 5, and the overall performance is summarized in Table 6. Despite involving fewer binary variables, the proposed distributed solution methodology closely matches the real-time load demand, leading to

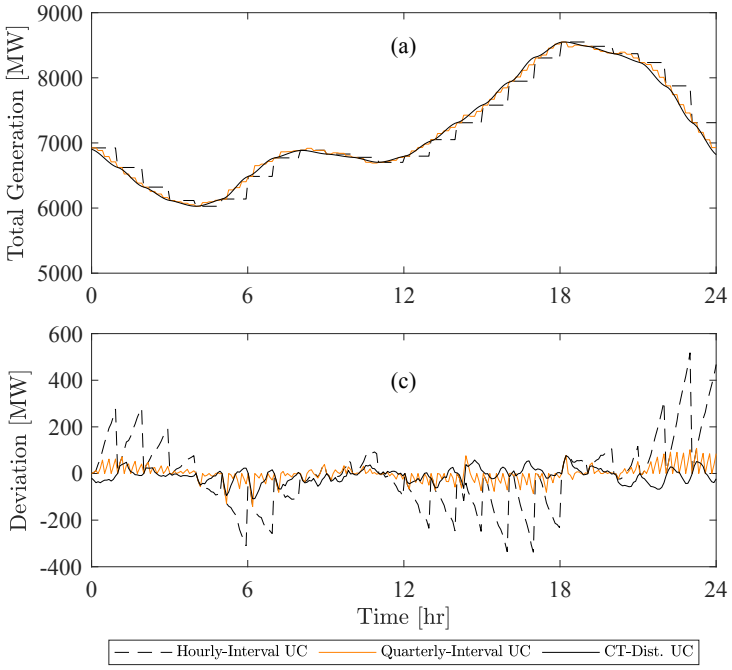

Figure 11: (a) Aggregate generation in IEEE-RTS solved from discrete-time UC models formulated with hourly and quarter-hourly intervals and from the proposed distributed continuous-time UC model, (b) Deviation of aggregate generation from real-time load profile in Fig. 5

lower real-time operational costs and a reduced need for ramping resources compared to discrete-time solutions.

5. Concluding Remarks

In this paper, we proposed a distributed solution for a variational multi-area UC problem incorporating energy storage. The multi-area UC problem was formulated as a variational optimization problem, followed by the projection of continuous-time parameter and decision trajectories into Bernstein function space, thereby forming a more computationally tractable MILP problem. We then decomposed the ensuing function space-based multi-area UC problem into per-area UC sub-problems that collectively reach an efficient interconnection power exchange through sharing limited information with a central coordinator, thus, preserving the local resource data privacy. The numerical results of implementing the proposed distributed solution on the

three-area IEEE-RTS demonstrate close matching between the distributed and centralized solutions via representative performance indices for operation cost and power schedules. In addition, the results highlight the sensitivity of the distributed continuous-time UC solution to ramping requirements in the system demand and its effectiveness in optimally scheduling the generating units and ES devices in areas with abundant ramping capability to serve demand in areas with limited ramping resources. The solution methodology was further tested on a larger six-area mirrored IEEE-RTS network, demonstrating its scalability, and compared with discrete-time solutions to emphasize its benefits. Future work will account for net demand uncertainty in developing distributed algorithms for the multi-area UC problem where the continuous-time generation and reserve are co-optimized and cover the aspects of real-time operations.

References

[1] The long-term strategy of the united states, pathways to net-zero greenhouse gas emissions by 2050, Tech. rep., U.S. Department of State and U.S. Executive Office of the President (2021).

[2] P. Donohoo-Vallett, N. Ryan, R. Wiser, On the path to 100% clean electricity, Tech. rep., U.S. Department of Energy (2023).

[3] L. Bird, M. Milligan, D. Lew, Integrating variable renewable energy: Challenges and solutions, Tech. rep., National Renewable Energy Lab.(NREL), Golden, CO (United States) (2013).

[4] J. Katz, M. Milligan, J. Cochran, Sources of operational flexibility, greening the grid, Tech. rep., National Renewable Energy Lab.(NREL), Golden, CO (United States) (2015).

[5] Updated GMI strategy, Tech. rep., US Department of Energy (2020).

[6] Grid modernization strategy, Tech. rep., US Department of Energy (2024).

[7] Ferc order no. 2222: A new day for distributed energy resources, Tech. rep., Federal Energy Regulatory Commission, Washington, DC, USA (2020).

[8] A report of the energy systems integration group's distributed energy resources task force, Tech. rep., Energy Systems Integration Group (Jan. 2022).

[9] Y. Chen, F. Pan, F. Qiu, A. S. Xavier, T. Zheng, M. Marwali, B. Knueven, Y. Guan, P. B. Luh, L. Wu, B. Yan, M. A. Bragin, H. Zhong, A. Giacomoni, R. Baldick, B. Gisin, Q. Gu, R. Philbrick, F. Li, Security-constrained unit commitment for electricity market: Modeling, solution methods, and future challenges, IEEE Transactions on Power Systems 38 (5) (2023) 4668–4681.

[10] F. Solzbacher, M. Parvania, R. Khatami, A. Bagherinezhad, B. Li, Stochastic continuous-time flexibility scheduling and pricing in wholesale electricity markets, Tech. rep., Univ. of Utah, Salt Lake City, UT (United States) (2021). doi:10.2172/1821121.

[11] Participation of distributed energy resource aggregations in markets operated by regional transmission organizations and independent system operators, Tech. rep., Federal Energy Regulatory Commission (2020).

[12] A. J. Wood, B. F. Wollenberg, G. B. Sheblé, Power generation, operation, and control, John Wiley & Sons, 2013.

[13] S. Pineda, R. Fernández-Blanco, J. M. Morales, Time-adaptive unit commitment, IEEE Trans. on Power Syst. 34 (5) (2019) 3869–3878.

[14] E. Ela, M. O'Malley, Studying the variability and uncertainty impacts of variable generation at multiple timescales, IEEE Transactions on Power Systems 27 (3) (2012) 1324–1333.

[15] B. Zhou, J. Fang, X. Ai, W. Yao, J. Wen, Flexibility-enhanced continuous-time scheduling of power system under wind uncertainties, IEEE Transactions on Sustainable Energy 12 (4) (2021) 2306–2320. doi:10.1109/TSTE.2021.3089696.

[16] L. Le, J. Fang, X. Ai, S. Cui, J. Wen, Aggregation and scheduling of multi-chiller hvac systems in continuous-time stochastic unit commitment for flexibility enhancement, IEEE Transactions on Smart Grid 14 (4) (2023) 2774–2785. doi:10.1109/TSG.2022.3227390.

[17] R. Philipsen, G. Morales-España, M. de Weerdt, L. De Vries, Trading power instead of energy in day-ahead electricity markets, Applied Energy 233 (2019) 802–815.

[18] M. Parvania, A. Scaglione, Unit commitment with continuous-time generation and ramping trajectory models, IEEE Trans. on Power Syst. 31 (4) (Jul. 2016) 3169–3178. doi:10.1109/TPWRS.2015.2479644.

[19] R. Khatami, M. Parvania, P. P. Khargonekar, Scheduling and pricing of energy generation and storage in power systems, IEEE Trans. on Power Syst. 33 (4) (Jul. 2018) 4308–4322.

[20] B. Li, A. Bagherinezhad, R. Khatami, M. Parvania, Continuous-time look-ahead optimization of energy storage in real-time balancing and regulation markets, IEEE Syst. Journal 15 (3) (2020) 3230–3237.

[21] R. Khatami, M. Parvania, Spatio-temporal value of energy storage in transmission networks, IEEE Syst. Journal 14 (3) (2020) 3855–3864.

[22] R. Khatami, M. Parvania, Continuous-time locational marginal price of electricity, IEEE Access 7 (2019) 129480–129493.

[23] A. Bose, T. J. Overbye, Electricity transmission system research and development: Grid operations, Tech. rep., US Department of Energy (2021).

[24] New England ISO, Dec. 2024. [link].
URL `https://www.iso-ne.com/`

[25] M. Franke, O. Stanojev, L. Mitridati, G. Hug, Privacy-preserving distributed market mechanism for active distribution networks, Electric Power Systems Research 234 (2024) 110616. doi:https://doi.org/10.1016/j.epsr.2024.110616.

[26] M. Hoseinpour, M. Hoseinpour, M. Haghifam, M.-R. Haghifam, Privacy-preserving and approximately truthful local electricity markets: A differentially private vcg mechanism, IEEE Transactions on Smart Grid 15 (2) (2024) 1991–2003. doi:10.1109/TSG.2023.3301174.

[27] A. Bagheri, S. Jadid, A robust distributed market-clearing model for multi-area power systems, International Journal of Electrical Power & Energy Systems 124 (2021) 106275. doi:https://doi.org/10.1016/j.ijepes.2020.106275.

[28] Y. Zhang, Q. Ai, H. Wang, Z. Li, K. Huang, Bi-level distributed day-ahead schedule for islanded multi-microgrids in a carbon trading market, Electric Power Systems Research 186 (2020) 106412. doi:https://doi.org/10.1016/j.epsr.2020.106412.

[29] C. Zhang, L. Yang, Distributed ac security-constrained unit commitment for multi-area interconnected power systems, Electric Power Systems Research 211 (2022) 108197. doi:https://doi.org/10.1016/j.epsr.2022.108197.

[30] W. Yamin, W. Shouxiang, W. Lei, Distributed optimization approaches for emerging power systems operation: A review, Electric Power Syst. Research 144 (2017) 127–135. doi:10.1016/j.epsr.2016.11.025.

[31] M. J. Feizollahi, M. Costley, S. Ahmed, S. Grijalva, Large-scale decentralized unit commitment, International Journal of Electrical Power and Energy Syst. 74 (2015) 97–106. doi:10.1016/j.ijepes.2015.04.009.

[32] A. Ahmadi-Khatir, A. J. Conejo, R. Cherkaoui, Multi-area unit scheduling and reserve allocation under wind power uncertainty, IEEE Trans. on Power Syst. 29 (4) (2014) 1701–1710. doi:10.1109/TPWRS.2013.2293542.

[33] A. Kargarian, Y. Fu, Z. Li, Distributed security-constrained unit commitment for large-scale power systems, IEEE Trans. on Power Syst. 30 (4) (2015) 1925–1936. doi:10.1109/TPWRS.2014.2360063.

[34] A. Kargarian, M. Mehrtash, B. Falahati, Decentralized implementation of unit commitment with analytical target cascading: A parallel approach, IEEE Trans. on Power Syst. 33 (4) (2018) 3981–3993. doi:10.1109/TPWRS.2017.2787645.

[35] B. Lamichhane, Y. C. Chen, R. Khatami, Distributed continuous-time optimal power flow, in: 2023 North American Power Symposium (NAPS), 2023, pp. 1–6. doi:10.1109/NAPS58826.2023.10318816.

[36] P. Dierckx, Curve and surface fitting with splines, Oxford University Press, 1995.

[37] P. M. Prenter, et al., Splines and variational methods, Courier Corporation, 2008.

[38] S. Tosserams, L. F. P. Etman, P. Y. Papalambros, J. E. Rooda, An augmented lagrangian relaxation for analytical target cascading using the alternating direction method of multipliers, Structural and Multidisciplinary Optimization 31 (3) (2006) 176–189.

[39] C. Grigg, P. Wong, P. Albrecht, R. Allan, M. Bhavaraju, R. Billinton, Q. Chen, C. Fong, S. Haddad, S. Kuruganty, et al., The IEEE reliability test system-1996. a report prepared by the reliability test system task force of the application of probability methods subcommittee, IEEE Trans. on power syst. 14 (3) (1999) 1010–1020.

[40] California ISO Operan Access Same-Time Information System, March. 2023. [link].
URL http://oasis.caiso.com

[41] R. Rosenthal, Gams—a user's guide, Tech. rep., GAMS Development Corp., Washington, DC, USA (2011).

[42] The ILOG CPLEX, 2019. [link].
URL http://www.ilog.com/products/cplex/

[43] Day-ahead market enhancements, Tech. rep., California ISO (2019).